

Resolving the Electron Transfer Kinetics in the Bacterial Reaction Center by Pulse Polarized 2-D Photon Echo Spectroscopy

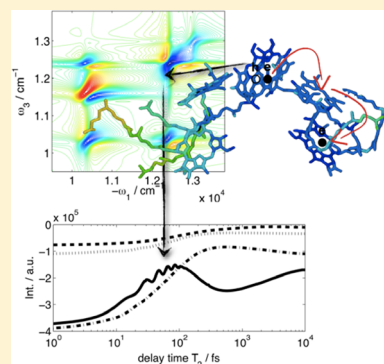
Benjamin P. Fingerhut* and Shaul Mukamel*

Chemistry Department, University of California, Irvine, California 92697-2025, United States

Supporting Information

ABSTRACT: At the heart of photosynthesis is excitation energy transfer toward and charge separation within highly conserved reaction centers (RCs). The function principles of RCs in purple bacteria offer a blueprint for an optoelectronic device, which efficiently utilizes the near-IR region of the solar spectrum. We present theoretical modeling of the nonlinear optical response of the bacterial RC *B. viridis* incorporating electron and energy transfer on equal footing. The splitting of special pair excitons P is the origin of distinct cross peaks, which allow monitoring of the kinetics of charge separation. The $xxyy - xyxy$ signal, obtained from sequences of orthogonal polarized laser pulses, highlights the kinetics of the secondary, subpicosecond electron transfer from the accessory bacteriochlorophyll BCl_L to the bacteriopheophytine BP_L . The increased selectivity is explained by the relative orientation of exciton transitions. The technique can resolve complex kinetics in congested signals of photosynthetic complexes that are otherwise hardly accessible.

SECTION: Energy Conversion and Storage; Energy and Charge Transport



In the reaction centers (RCs) of purple bacteria and plants, excitation energy transfer (EET) triggers a charge separation (CS) cascade that transforms the energy of sunlight into a chemical potential gradient. Both EET and CS proceed with near-unity efficiency,¹ and the understanding of these ultrafast initial photosynthetic steps may help for the design of artificial photochemical devices. While the RCs of higher plants operate at high band gaps (680–700 nm) and drastic redox potentials, allowing for the unique water splitting capabilities, the RCs of purple bacteria absorb light in the near-IR region (860–980 nm) of the incident solar spectrum. The utilization of the low-energy region of solar radiation is required for the construction of photochemical devices with highest energy conversion efficiencies.^{2–4} Recent developments in laser technology allow one to follow the initial photosynthetic steps on an ultrafast time scale. Coherent 2D nonlinear optical spectroscopy provides up to date the most comprehensive picture by directly monitoring the couplings between chromophores and distinct energy transfer pathways.⁵

We present simulations of the 2D photon echo (PE) spectra of the bacterial RC *Blastochloris (B.) viridis*, which reveal the kinetics of EET coupled to the CS cascade. Two signals obtained from different pulse polarization configurations are considered; in the first, all pulses are x -polarized ($xxxx$) in an all-parallel (AP) configuration, whereas the second is the cross-polarized ($CP = xxyy - xyxy$) signal, which is composed of two of the three independent tensor components $xxxx = xxyy + xyxy + xyyx$, and orthogonal polarized pulses are used ($i = x, y, z$ denotes the lab frame polarization direction). The simulations are based on a tight-binding electronic Hamiltonian⁶ and the X-ray structural data^{7,8} of *B. viridis*. The chromophores in the RC

are positioned with approximate two-fold symmetry in two branches (Figure 1, right). Two strongly coupled bacteriochlorophylls (BCl) form the special pair P, the CS occurs over the active L branch in a primary electron transfer (ET) reaction from P to the accessory BCl_L on the low picosecond time scale, followed by a faster secondary ET from BCl_L to bacteriopheophytine (BP_L) on the subpicosecond time scale.^{9–11} We focus on the Q_s band of BCls and BPs and take into account EET over all six chromophores and CS over the active L branch of the RC (Figure 1, bottom). Under natural conditions, virtually all excitation energy is funneled from antenna systems toward the RC and initiates the CS at the special pair P.^{12,13} We thus focus on this predominant route for CS. The microscopic calculation of the transport uses a generalized Redfield rate expression^{6,14} that is nonperturbative in the diagonal fluctuations,¹⁵ accounting for the strong coupling of charge transfer (CT) states with the bath (for details of the model, see the Theoretical Methods section), which recovers the Marcus theory for localized excitons and includes polaron effects (reorganization). This allows one to describe EET and CS on equal footing.

The calculated absorption spectrum of *B. viridis* is shown in Figure 2a, right in the temperature range of 50–295 K and serves as a benchmark of the optical active molecular excitations (MEs). The MEs form two distinct exciton bands with a low-energy ~980 nm absorption and a higher-energy ~800 nm exciton band. The lowest-energy absorption P^- (980 nm,

Received: May 17, 2012

Accepted: June 15, 2012

Published: June 18, 2012

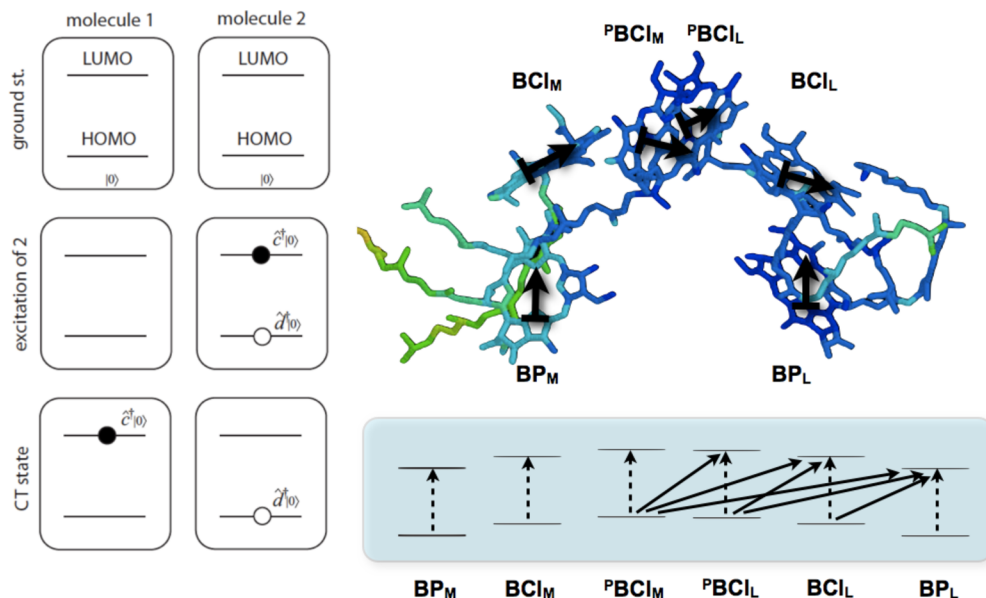


Figure 1. RC model of *B. viridis*: On site tight-binding model (left) and chromophores in the RC (right). The orientation of the site transition dipole is indicated with black arrows. The considered optically allowed chromophore excitations are indicated with dashed arrows, and charge-separated states are indicated with solid arrows (right bottom).

excitons are highlighted in bold throughout the Letter) arises from the negative linear combination of the special pair P^+BCI_M and P^-BCI_L transitions. Exciton delocalization is characterized by the inverse participation ratio L_e^{16} (which reaches values between 1 for localized and the number of sites N for completely delocalized states; Table 1); for P^- , we find $L_e =$

occurs to BP_L (0.04%) and the special pair molecules (0.04%). The asymmetry of the unidirectional CS cascade on the L branch in bacterial RCs is thus already reflected in the composition of the P^+ and BCI_L excitons. In the investigated temperature range, we find good agreement with the experimental absorption spectrum (Figure 2a, left)¹⁰ in both the position and shape of the prominent Q_σ absorption bands. Special attention is given to the unusual temperature dependence of the P^- absorption band (980 nm) that arises from the coupling to CT states.¹⁷ We observe a blue shift and broadening with increasing temperature, similar to that from experiment.

The CT states (excitons 1–4 in Table 1) are localized, with $PBCI_L^+BP_L^-$ being lowest in energy (BP_L^-), followed by $PBCI_L^+BCI_L^-$ (BCI_L^-). Weak delocalization occurs due to the contribution of different hole states from the special pair molecules $PBCI_M$ and $PBCI_L$ ($L_e = 1.15$ and 1.13, respectively). The population dynamics of dark CT states is analyzed by solving the rate equation system with the individual EET and CS rates calculated microscopically (see Supporting Information (SI-eqs 9–11)). As initial conditions, we assume that the P^- state is populated at $t = 0$, allowing one to compare the kinetics to donor-bridge-acceptor models for CS in RCs from $PBCI$ via BCI_L to BP_L .^{18–20} Our simulations (Figure 2b) additionally include ME states and a realistic description of the electron and hole particle states, which doubles the number of CT states (the hole can reside on $PBCI_L$ and $PBCI_M$). The combined special pair decay ($P^- + P^+$) (red line in Figure 2b) is nonexponential with a mean time constant of about 3 ps. The ME states P^+ and BCI_L are weakly populated on the subpicosecond time scale due to EET. The lowest-energy CT state BP_L^- (with $PBCI_M^+BP_L^-$ character) is populated on the low picosecond time scale, resembling the decay of the special pair. The BCI_L^- state is intermediately populated (~20%), and the population shows up almost entirely in the $PBCI_L^+BCI_L^-$ biradical (green lines in Figure 2b; hole transfer between $PBCI$ molecules is faster than $PBCI \rightarrow BCI_L^-$ ET). The transient BCI_L^- population reaches a maximum at ~1.8 ps. The simulated kinetics

Table 1. Character (CT or ME) and Dominant Configuration to the n th Exciton and Inverse Participation Ratio $L_e = (1/\sum_n |\Psi_{en}|^4)^{1/2}$

exciton	character	dominant configuration	L_e
1	(BP_L^-)	CT	0.93 $PBCI_L^+BP_L^-$ + 0.04 $PBCI_M^+BP_L^-$
2	(BCI_L^-)	CT	0.94 $PBCI_L^+BCI_L^-$ + 0.03 $PBCI_M^+BCI_L^-$
3		CT	0.94 $PBCI_M^+BP_L^-$ + 0.04 $PBCI_L^+BP_L^-$
4		CT	0.95 $PBCI_M^+BCI_L^-$ + 0.03 $PBCI_L^+BCI_L^-$
5	(P^-)	ME	0.50 $PBCI_L$ + 0.50 $PBCI_M$
6	(P^+)	ME	0.44 $PBCI_L$ + 0.44 $PBCI_M$
7	(BCI_L)	ME	0.73 BCI_L + 0.21 BCI_M
8	(BCI_M)	ME	0.75 BCI_M + 0.15 BCI_L
9	(BP_L)	ME	0.96 BP_L + 0.04 BCI_L
10	(BP_M)	ME	0.99 BP_M
11		CT	0.99 $PBCI_M^+BCI_L^-$
12		CT	0.99 $BCI_L^+BP_L^-$

^aThe label of the excitons is given in parentheses.

2.03. The P^+ exciton shows up as a weak shoulder at 850 nm and corresponds to the most delocalized state ($L_e = 2.53$) arising from the special pair molecules $PBCI_M$ and $PBCI_L$ and additional contributions of the BCI_L site; the BCI_M contribution is minor. The individual Q_σ transitions of the BCI_L and BCI_M (795–835 nm) and BP_L/BCI_L chromophores (760–780 nm) contributing to the high-energy exciton band (760–840 nm) can be identified at low temperature (50–130 K). A broad and unstructured absorption band shows up at ambient temperatures (180–295 K). The highest-intensity exciton BCI_L (795–805 nm) shows the predominant contribution from the BCI_L site (0.73%), followed by BCI_M (0.21%); further delocalization

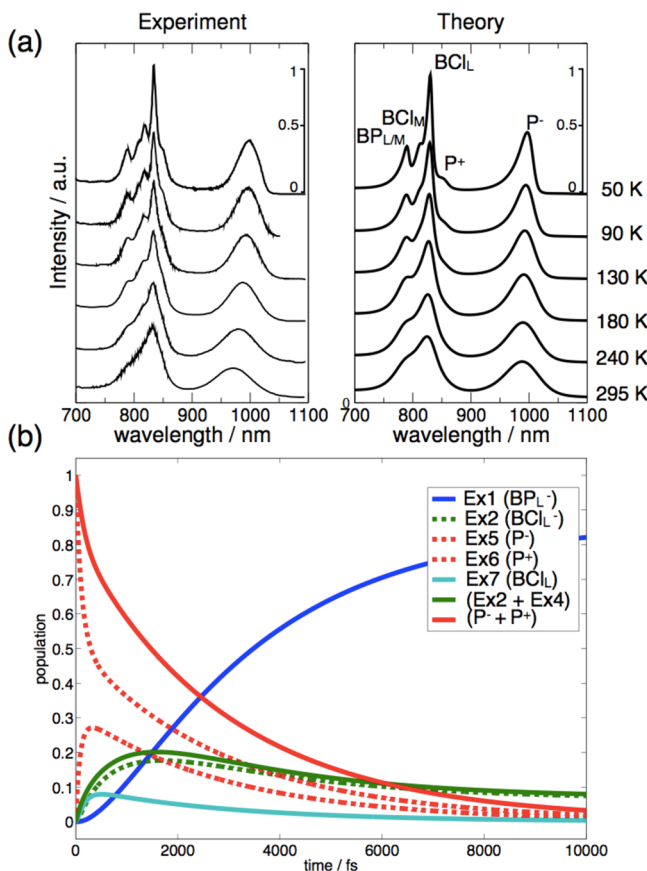


Figure 2. (a) Experimental¹⁰ (left) and simulated (right) temperature-dependent absorption spectrum of the RC *B. viridis*. (b) Simulated population dynamics of CS. The leading configuration of exciton states is given in parentheses. The spectra are normalized to the maximum absorption at $T = 50$ K, and the same scale bar applies to the offset spectra at the indicated temperatures.

resembles closely the experimentally observed^{9,10} and simulated^{18–20} kinetics in *B. viridis*. We find that the kinetics of primary CS shows up in the population of the BP_L^- state. The initial ${}^{\text{P}}\text{BCl}^+\text{BCl}_\text{L}$ CS occurs on the low picosecond time scale, followed by a secondary ET reaction ${}^{\text{P}}\text{BCl}^+\text{BCl}_\text{L}\text{BP}_\text{L} \rightarrow {}^{\text{P}}\text{BCl}^+\text{BCl}_\text{L}\text{BP}_\text{L}^-$ on the subpicosecond time scale. The kinetics of the faster secondary ET shows up in the rise of the BCl_L^- population.

We propose two 2D-PE signals involving different pulse polarization configurations to monitor the dynamics in *B. viridis*. In the first all-parallel (AP) configuration, all pulses are x -polarized ($xxxx$); in the second cross-polarized (CP = $xxyy$ – $xyxy$) configuration, orthogonal polarized pulses are used, and two of the three independent tensor components of the signal $xxxx = xxyy + xyxy + xyyx$ are monitored ($i = x, y, z$ denotes the lab frame polarization direction). The difference of the signals can be explained by their different contributions to the third-order response

$$S_i^{(3)} = G_i(t_3, t_2, t_1) \times M_i \quad (1)$$

for an individual quantum pathway i (the respective ladder diagrams are depicted in the SI-Figure 1). Here, G_i describes the exciton dynamics containing the system dynamics of excited-state emission (ESE), ground-state bleach (GSB), or excited-state absorption (ESA). M_i denotes the geometry-dependent amplitude for a given optical pulse polarization

configuration. At $t_2 = 0$, the signal $S^{(3)}$ is invariant to the interchange of the second and third pulses; a permutation interchanges ESE and GSB contributions but leaves the ESA unaffected. As a consequence of this symmetry, the signal $\text{CP} = S_{\text{xxyy}}^{(3)}(\Omega_3, t_2, \Omega_1) - S_{\text{xyxy}}^{(3)}(\Omega_3, t_2, \Omega_1)$ vanishes at $t_2 = 0$. For $t_2 \neq 0$, the system quantum dynamics affects the population pathways (pp) ESE and ESA, whereas the GSB does not evolve. The symmetry breaking between quantum pathways leads to a gradual increase in the CP signal intensity (see Figure 4c for $t_2 > 0$), highlighting dynamic features²¹ like coherent evolution on short time scales and population dynamics on longer time scales. t_2 -independent signal features are suppressed by symmetry.

The geometry-dependent amplitudes M_i control the signal intensities. For both pp, the first two interactions create a doorway wavepacket d, and the third and fourth interactions act on the window wavepacket w. For an ensemble of randomly oriented molecules in the dipole approximation, the orientationally averaged amplitudes $\langle M_i \rangle = \langle \mu_w^{\nu_4} \mu_w^{\nu_3} \mu_d^{\nu_2} \mu_d^{\nu_1} \rangle$ for the three independent tensor components $xxxx = xxyy + xyxy + xyyx$ are given by^{22,21}

$$\begin{aligned} \langle M_{i,\text{pp}}(xxyy) \rangle &= \frac{2}{30}(2\mu_w^2 \mu_d^2 - (\mu_w \cdot \mu_d)) \\ \langle M_{i,\text{pp}}(xyxy) \rangle &= \langle M_{i,\text{pp}}(xyyx) \rangle = \frac{1}{30}(-\mu_w^2 \mu_d^2 + 3(\mu_w \cdot \mu_d)) \end{aligned} \quad (2)$$

and depend on the relative angle between the d and w exciton dipole transitions ($\mu_w \cdot \mu_d$). For parallel orientation of μ_w and μ_d , the orientational averaged amplitudes $\langle M_i \rangle$ of the CP signal exactly cancel. For orthogonal μ_w and μ_d , the amplitude $\langle M_i \rangle$ of the CP signal is maximal. In the $xxxx$ configuration, the signal intensity is maximal for parallel orientation of μ_w and μ_d and minimal for orthogonal μ_w and μ_d .

Energy Transfer and CS in the xxxx 2D-PE Signal. Simulated $xxxx$ 2D-PE spectra of the RC *B. viridis* are shown in Figure 3. In all simulations, Gaussian laser pulses centered at 12150 cm^{-1} with a bandwidth of 2400 cm^{-1} (6.1 fs fwhm) are used to cover the complete Q_y exciton band and monitor the third-order response of the material.¹⁶ Along the diagonal, we find pronounced negative features. At low energy ($-\omega_1 = 10500 \text{ cm}^{-1}$), the P^- absorption is spectrally resolved. The high-energy band ($-\omega_1 = 12000\text{--}13000 \text{ cm}^{-1}$) is composed of contributions from the P^+ , BCl , and BP excitons.

The spectrally separated P^- exciton gives rise to off-diagonal features in the 2D-PE spectra of *B. viridis*. In the 2D correlation plot, $|\text{g}\rangle\langle\text{el}|$ coherences of the density matrix appear along the $-\omega_1$ axis, and $|\text{e}'\rangle\langle\text{gl}|$ and $|\text{l}\rangle\langle\text{el}|$ coherences appear along the ω_3 axis (with the ground state g, the single exciton manifold e and the biexcitons manifold f; for contributing ladder diagrams see SI-Figure 1 in the Supporting Information). The resulting cross peaks reveal correlations between different excitons. We find a rich structure of cross peaks, and prominent features can be identified between P^- and BCl_L excitons ($-\omega_1 = 10500 \text{ cm}^{-1}$, $\omega_1 = 12300 \text{ cm}^{-1}$). The P^- – BCl_L cross peak shows up symmetric to the diagonal in both half planes of the spectrum (P^- – BCl_L and BCl_L – P^- in Figure 3a). An additional cross peak shows up only in the upper half plane of the spectrum ($-\omega_1 = 10500 \text{ cm}^{-1}$, $\omega_3 = 11900 \text{ cm}^{-1}$), which arises from ESA contributions to the signal (P_{ESA}^-). Because only the P^- exciton has a strong transition moment (compare Figure 3a), the corresponding P^+ cross peak ($-\omega_1 = 11950 \text{ cm}^{-1}$) can be

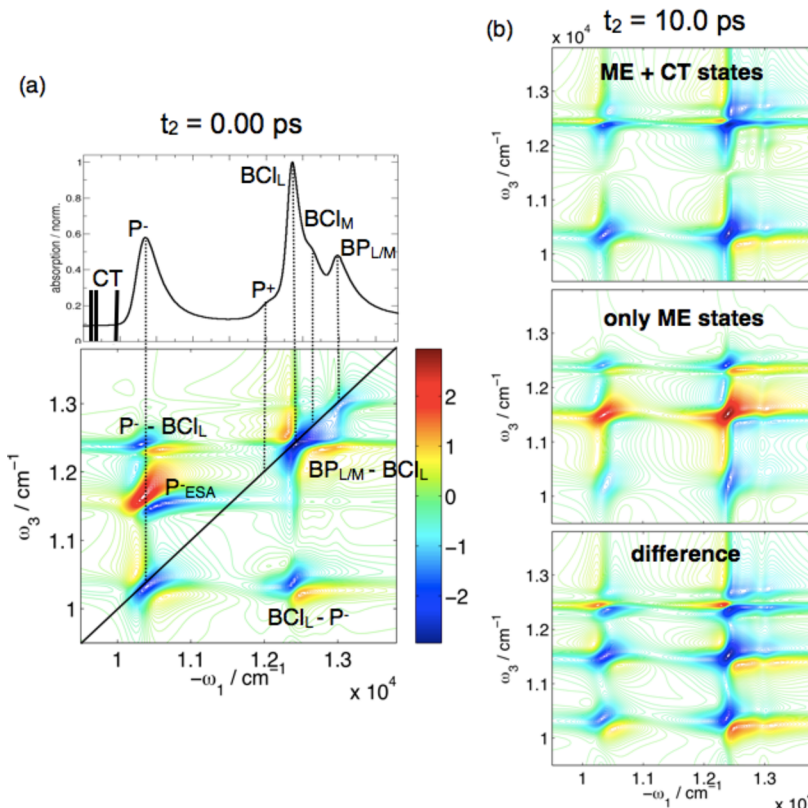


Figure 3. Calculated imaginary part of the 2D-PE signal of *B. viridis* for *xxxx*-polarized pulses at $T = 77$ K: (a) $t_2 = 0.00$ ps. Sticks mark the positions of CT states. The lowest-energy CT state BCl_L^- is outside of the depicted frequency range. (b) Spectral features arising from contributions of the CT states. (Top) 2D-PE spectrum of the complete Hamiltonian (SI-Table 1, Supporting Information) for $t_2 = 10$ ps; (middle) only optically allowed MEs; (bottom) difference of both spectra. All signals are displayed on the nonlinear scale given by SI-eq 14 (Supporting Information).

identified only as weak shoulder of the intense $\text{BCl}_L^- - \text{P}^-$ cross peak. Additional less pronounced cross peaks show up near the diagonal and arise from the coherences of BCl and BP excitons ($-\omega_1 = 12600\text{ cm}^{-1}$, $\omega_3 = 12300\text{ cm}^{-1}$).

Additional reference calculations with a truncated Hamiltonian, only including the bright ME states were performed to identify clear signatures of the CT states in 2D-PE spectra. At long t_2 times, characteristic signatures of CT states can be identified (Figure 3b), whereas at $t_2 = 0.00$ ps, the 2D-PE spectra are equal for both models (data not shown). The spectra of the complete model (ME + CT states; Figure 3b, top) are dominated by strong negative signal features at long delay times, which arise from the depopulation of the bright ME states and the population of the dark CT states. A prominent bleach component can be identified at ($-\omega_1 = 12300\text{ cm}^{-1}$, $\omega_3 = 10500\text{ cm}^{-1}$), and slightly shifted ($\omega_3 = 10200\text{ cm}^{-1}$) positive signal intensities show up. The 2D-PE spectra of the reduced model (only ME states; Figure 3b, middle) shows pronounced cross peaks with positive amplitude due to energy transfer toward lower exciton states (e.g., $-\omega_1 = 12300\text{ cm}^{-1}$, $\omega_3 = 11800\text{ cm}^{-1}$), while the bleaching of the P^- exciton is substantially reduced. In the difference spectra (Figure 3b, bottom), negative contributions highlight the bleaching due to the population of CT states. Positive features as direct signatures of CT states appear red-shifted to the strong bleaching components. The population of the CT states controls the bleach and bleach recovery of bright ME states and is essential for a realistic simulation of population transfer in RCs.

The population dynamics of the RC obtained from the *xxxx* pulse configuration is inspected by monitoring the evolution of diagonal and cross peaks for different t_2 times; the respective peaks are indicated in snapshots of the 2D-PE spectra shown in Figure 4a. The dynamics of the diagonal and cross peaks (Figure 4b, top and bottom) can be classified into three time periods: within the first 100 fs, oscillatory energy migration of exciton wavepackets can be observed; after 100 fs, the oscillatory motion is damped; and EET toward lower energy exciton states occurs on the sub-500 fs time scale. Later on, we observe a slower redistribution of peak intensities on the low picosecond time scale.

The population dynamics of the diagonal peaks P^- , BCl_L^- , and $\text{BP}_{L/M}$ (Figure 4b, top) is similar within the first 200 fs and shows a bleach recovery due to the decay of the ESE contribution to the signal. Later on, different kinetic phases show up in the diagonal peaks. In contrast, the P^+ diagonal peak with weak intensity shows contributions from exciton wavepackets for $t_2 < 100$ fs. Later on, the P^+ peak intensity decreases ($t_2 < 500$ fs), followed by a bleach recovery on the low picosecond time scale. The time evolution of cross peaks (Figure 4b, bottom) monitors the energy dissipation between exciton states. Initially, the cross peaks $\text{BCl}_L^- - \text{P}^-$, $\text{P}^- - \text{BCl}_L^-$, P_{ESA}^- , and BCl_L^- show a strong oscillatory time evolution ($t_2 < 100$ fs). The oscillation of BCl_L^- and $\text{BCl}_L^- - \text{P}^-$ are anticorrelated, whereas $\text{P}^- - \text{BCl}_L^-$ shows a relative phase shift. Later on ($t_2 < 500$ fs), EET leads to an increase of the cross peak $\text{BCl}_{L,\text{ESA}}$ due to energy dissipation from BCl_L^- to P^+ . The initially dark $\text{BCl}_{L,\text{ESA}}$ signature lightens up during the dynamics and becomes the most intense off-diagonal feature. On the low

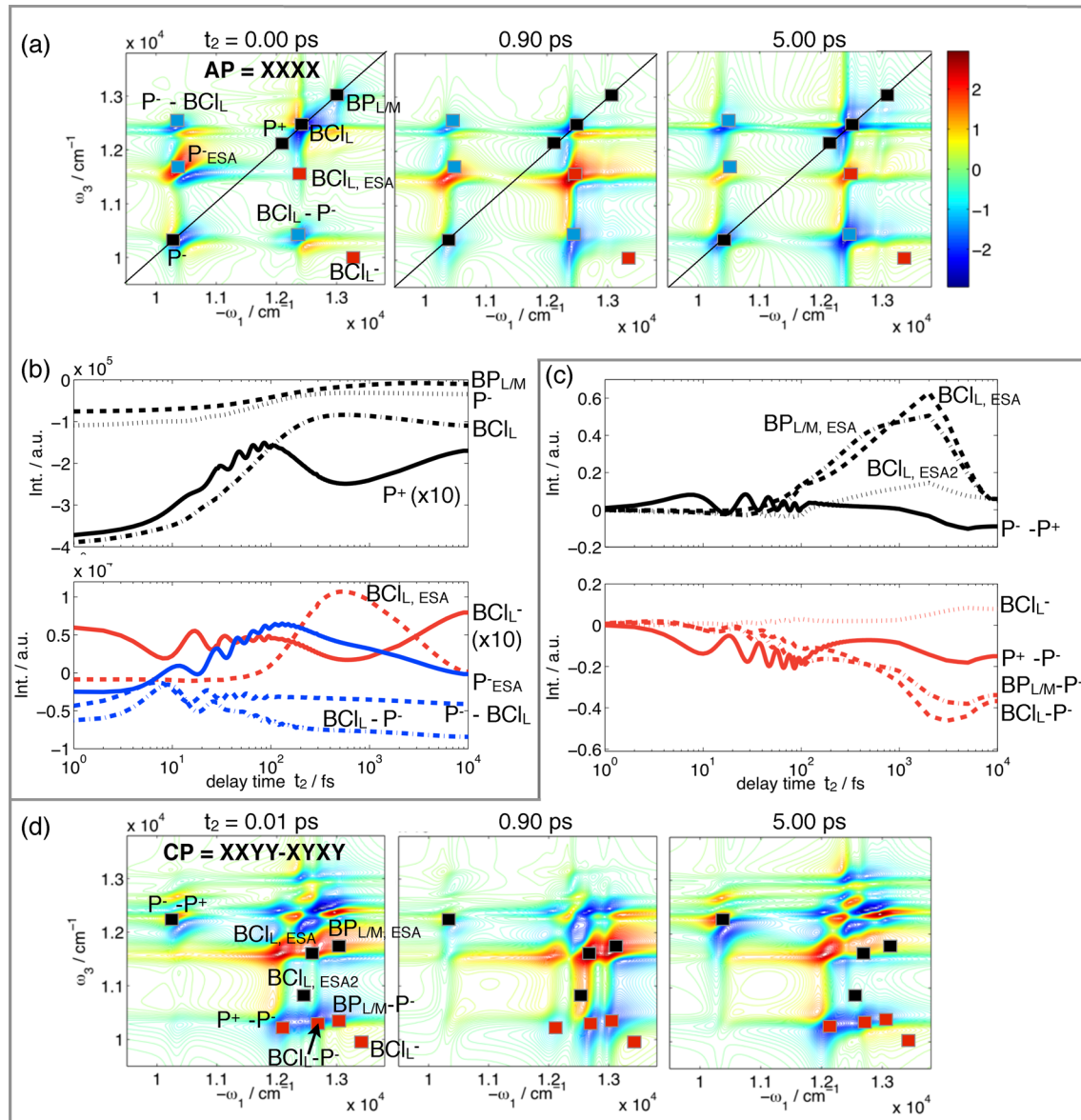


Figure 4. Kinetic components extracted from the simulated 2D-PE spectra of RC *B. viridis* (77 K): (a) xxxx-polarized pulses and (d) the linear combination signal CP = xxxy – xyxy. By varying the delay time t_2 , the population dynamics of the indicated peaks is monitored (b and c).

picosecond time scale, the cross peak intensity is reduced, and we assign this decrease to the depopulation of the bright ME states of the special pair along with the population of dark CT states. The time evolution of the BCl_L^- cross peak, characteristic for the signatures of CT states (compare Figure 3), mirrors the $\text{BCl}_{L,\text{ESA}}$ decay. At long delay times ($t_2 > 1 \text{ ps}$), the BCl_L^- cross peak shows positive signal intensity reflecting the population of the CT states. The associated time constant (showing up in cross peaks $\text{BCl}_{L,\text{ESA}}$ and BCl_L^-) is on the low picosecond time scale and highlights the initial ${}^{\text{P}}\text{BCl}_L \rightarrow {}^{\text{P}}\text{BCl}^+\text{BCl}_L^-$ CS. From the xxxx-polarized 2D-PE spectra, the kinetics of the faster secondary ET step ($\sim 0.9 \text{ ps}$) is not observable.

Secondary ET Observed in the CP = xxxy – xyxy 2D-PE Signal. This signal (Figure 4d) shows profound differences compared to the xxxx configuration. Additional cross peaks are identified that have the highest intensity; diagonal peaks contribute only weakly. At the position of the dominant $\text{BCl}_{L,\text{ESA}}$ cross peak ($\omega_3 = 12700 \text{ cm}^{-1}$), now distinct cross peaks can be identified, which originate from BCl_L and $\text{BP}_{L/M}$ excitons, respectively.

($\text{BCl}_{L,\text{ESA}}$ and $\text{BP}_{L/M,\text{ESA}}$ at $-\omega_1 = 12600$ and 13000 cm^{-1}). The same pattern is identified at lower ω_3 frequencies, with negative signal intensity ($\omega_3 = 10500 \text{ cm}^{-1}$) arising from coherences with the P^- exciton ($\text{P}^+ - \text{P}^-$, $\text{BCl}_L - \text{P}^-$, and $\text{BP}_{L/M} - \text{P}^-$).

Population dynamics (Figure 4c) of the $\text{P}^+ - \text{P}^-$ and $\text{P}^- - \text{P}^+$ cross peaks reveals pronounced wavepacket motion with anticorrelated phase; later on ($t_2 > 100 \text{ fs}$), both cross peaks decay. The $\text{BCl}_{L,\text{ESA}}$ and $\text{BP}_{L/M,\text{ESA}}$ signatures ($\omega_3 = 12700 \text{ cm}^{-1}$) show significant population dynamics with an intensity increase until $t_2 \approx 2 \text{ ps}$ and then further decays. Similar kinetics shows up in the cross peaks $\text{BCl}_L - \text{P}^-$ and $\text{BP}_{L/M} - \text{P}^-$ as initial decay and bleach recovery at later times. Furthermore, we identify the build up of an elongated spectral feature for $\text{BCl}_{L,\text{ESA2}}$ along ω_3 at the BCl_L exciton resonance ($-\omega_1 = 12400 \text{ cm}^{-1}$), which shows similar dynamics.

The kinetics of the AP and the CP signals show pronounced differences; the signatures of initial energy dissipation ($t_2 < 500 \text{ fs}$) are suppressed, and instead, the signal intensities peak at $t_2 \approx 2 \text{ ps}$ and mirror the transient population of the primary CT

state ${}^P\text{BCl}^+\text{BCl}_L^-$ (compare Figure 2). The kinetics of the secondary subpicosecond ET reaction shows up exclusively in the CP signal increase until $t_2 \approx 2$ ps. The selectivity for different kinetic phases can be explained from the contributions to the orientationally averaged amplitudes $\langle M_i \rangle = \langle \mu_w^{v_1} \mu_w^{v_2} \mu_d^{v_3} \mu_d^{v_4} \rangle$. In particular, we find that the P^- and BCl_L exciton transitions are approximately parallel (12.6°), whereas the P^- and BP_L transitions, as well as the BCl_L and BP_L transitions, possess nearly perfect orthogonal orientation (88.1 and 91.0° , respectively). The CP signal highlights the dynamics, where doorway d wavepackets correspond to P^- and BCl_L excitons, and the window w wavepacket corresponds to the BP_L exciton. As direct tunneling from P^- to BP_L (the superexchange mechanism) is strongly unfavored,^{18,19} the kinetics of the secondary ET $\text{BCl}_L^- \text{BP}_L \rightarrow \text{BCl}_L \text{BP}_L^-$ shows up in CP. The primary ${}^P\text{BCl} \text{BCl}_L \rightarrow {}^P\text{BCl}^+ \text{BCl}_L^-$ CS dynamics and diagonal signal features are efficiently suppressed.^{21,23} In contrast, in the $xxxx$ configuration, the highest intensity of cross peaks is observed for w and d wavepackets with relative parallel orientation ($\text{BCl}_L \rightarrow \text{P}^-$, $\text{P}^- \rightarrow \text{BCl}_L^-$), whereas the kinetic contributions from secondary ET are weak. Both methods thus allow one to extract highly complementary information about the dynamics in bacterial RCs. In contrast to measurements on single aligned crystals,²⁴ the ensemble effects of the orientationally averaged amplitudes $\langle M_i \rangle$ control the signal intensity and sensitivity.

In summary, we have presented a model of the bacterial RC *B. viridis* that incorporates the molecular excitations as well as CS on equal footing. This allowed for the simulation of nonlinear optical signals of the RC kinetics where EET is directly coupled to the CS steps. The RC model is benchmarked against the temperature-dependent absorption spectrum of *B. viridis* as well as the dynamics of CS and shows good agreement to reported data.^{9,10,18,19} We analyzed the 2D-PE signals for two pulse polarization configurations (AP and CP). The kinetics of excitation energy dissipation (the sub-500 fs component) and subsequent ${}^P\text{BCl} \text{BCl}_L \rightarrow {}^P\text{BCl}^+ \text{BCl}_L^-$ CS on the low picosecond time scale are revealed by the AP signal. The CS kinetics can be directly deduced from the evolution of cross peaks. In contrast, the CP signal highlights the secondary $\text{BCl}_L^- \text{BP}_L \rightarrow \text{BCl}_L \text{BP}_L^-$ ET kinetics. Both signals yield complementary information, where the selectivity is explained on the molecular level by the relative orientation of the exciton transition moments. Rotational averaging guarantees highest intensities for the CP signal if the transition moments between doorway and window wavepackets have orthogonal orientation. The unique arrangement of chromophores in the active L branch almost perfectly meets this requirement.

The high selectivity of the AP and CP signal leverages 2D electronic spectroscopy by revealing comprehensive information about energy relaxation pathways and the CS mechanism. The simulations envision the complete energy relaxation pathway from the time evolution of cross peaks. A coherent initial wavepacket motion is followed by “ballistic” energy relaxation toward the lowest exciton state P^- within the first 500 fs and precede the CS process. Additionally, secondary ET is directly accessed in the CP configuration, which poses challenges to conventional pump–probe spectroscopy^{9,10} and 2D electronic spectroscopy in the AP configuration.²⁵ Hereby, the cofactor-specific information about primary CS and secondary ET is obtained from the selection rules of the orientationally averaged amplitudes of the ensemble without the need for measurements on single crystals.²⁴

For the RC *B. viridis*, we find demanding requirements on the laser pulse bandwidth to cover the complete Q_γ exciton band. The spectrally resolved P^- transition is the origin of pronounced cross peaks, allowing one to follow the dynamics in detail. Comparison of different purple bacteria organisms shows that the spectral position of P^- varies (e.g., 860 nm for *Rb. sphaeroides*), allowing for reduced requirements on the laser pulses but preserving the basic cross peak pattern. Analysis of PS I^{26,27} and PS II^{6,28,29} reveals that the due to the highly preserved RC structure, similar relative orientations of exciton transitions are found in all three RCs. This unique feature and the experimental realization within reach^{25,30,31} make the strategy to extract complementary information from parallel and orthogonal pulse configurations a promising tool to dissect the complex population dynamics and interfering CS pathways^{12,29,32} in different RCs.

THEORETICAL METHODS

The developed model of *B. viridis* relies on a tight-binding formulation of the electronic Hamiltonian H_S ⁶ incorporating chromophore excitations and charge-separated states (Figure 1, left). H_S includes electron (hole) hopping amplitudes $t_{mn}^{(1/2)}$, the dipole–dipole coupling $W_{mn}^{(f)}$, and Coulomb interaction $W_{mn}^{(c)}$ between electron–hole pairs, as well as the electron–electron (hole–hole) repulsion $V_{mn}^{(1/2)}$. The matrix elements of single exciton states (one electron and one hole) $|e_m h_n\rangle = c_m^\dagger d_n^\dagger |0\rangle$ are given by

$$\begin{aligned} \langle e_m h_n | H_S | e_k h_l \rangle = & \delta_{nl} t_{mk}^{(1)} + \delta_{mk} t_{nl}^{(2)} + \delta_{kl} \delta_{mn} (1 - \delta_{mk}) W_{mk}^{(f)} \\ & - \delta_{mk} \delta_{nl} W_{mn}^{(c)} \end{aligned} \quad (3)$$

The model reduces to the Frenkel exciton model if only on-site excitations are considered. The physical description of the Coulomb interaction between charge carriers guarantees a proper description of all considered states and allows for the calculation of the two-exciton manifold (SI-eq 3, Supporting Information). The construction of H_S uses X-ray structural data of *B. viridis* (PDB code: 1PRC),⁸ and the Q_γ transition dipole moments are placed at the center of bacteriochlorophylls (${}^P\text{BCl}_M$, ${}^P\text{BCl}_L$, BCl_L , BCl_M) and bacteriopheophytines (BP_L , BP_M). The direction of the transition dipole moments is assumed to be in the direction of the pyrrole rings B and D.³³ The site excitation energies of BCls and BPs are taken from ref 34, and Förster couplings $W^{(f)}$ are calculated in the dipole approximation, except for the special pair ${}^P\text{BCl}_M$ and ${}^P\text{BCl}_L$, where a value of 852 cm^{-1} was chosen, allowing to reproduce the CD spectra of *B. viridis*.³⁴ By fixing the energies of the primary CT state ${}^P\text{BCl}^+ \text{BCl}_L^-$ relative to the special pair exciton state P^- ,^{35,36} we obtain a reference point that determines the energies of the additional CT states of the active L branch.⁶ The complete Hamilton matrix and a detailed discussion of all parameters is given in SI-Table 1 (Supporting Information). The exciton eigenstates are obtained by diagonalizing the single and double excited Hamilton matrix.

Transport between exciton states is induced by bath fluctuations. We model the RC spectral density by coupling the electron and hole sites to five harmonic bath modes; for the special pair, two additional low-frequency modes are used,³⁴ the bath parameters are given in the Supporting Information. The transport rates are calculated using a generalized Redfield rate expression¹⁴ for the energy and charge hopping that incorporates diagonal fluctuations nonperturbatively^{6,15} and accounts for the strong coupling of CT states with the bath.

The 2D-PE signal in the direction $k_l = -k_1 + k_2 + k_3$ is calculated by summing over the different quantum pathways in the eigenstate basis (eqs 141–145 of ref 16) to simulate the time domain third-order response function. The respective ladder diagrams are depicted in SI-Figure 1 (Supporting Information).

ASSOCIATED CONTENT

Supporting Information

Hamilton matrix, bath parameters, generalized Redfield rate expression, and tight-binding formulation of the electronic Hamiltonian H_S for single and double excited states. This material is available free of charge via the Internet at <http://pubs.acs.org>.

AUTHOR INFORMATION

Corresponding Author

*E-mail: bfingerh@uci.edu (B.P.F.); smukamel@uci.edu (S.M.).

Notes

The authors declare no competing financial interest.

ACKNOWLEDGMENTS

The support of the Chemical Sciences, Geosciences and Biosciences Division, Office of Basic Energy Sciences, Office of Science, U.S. Department of Energy is gratefully acknowledged. We also gratefully acknowledge the support of the National Science Foundation through Grants CHE-1058791 and CHE-0840513. B.P.F. gratefully acknowledges support from the Alexander-von-Humboldt Foundation through the Feodor Lynen program.

REFERENCES

- (1) Strümpfer, J.; Sener, M.; Schulten, K. How Quantum Coherence Assists Photosynthetic Light-Harvesting. *J. Phys. Chem. Lett.* **2012**, *3*, 536–542.
- (2) Shockley, W.; Queisser, H. J. Detailed Balance Limit of Efficiency of p–n Junction Solar Cells. *J. Appl. Phys.* **1961**, *32*, 510–519.
- (3) Fingerhut, B. P.; Zinth, W.; de Vivie-Riedle, R. The Detailed Balance Limit of Photochemical Energy Conversion. *Phys. Chem. Chem. Phys.* **2010**, *12*, 422–432.
- (4) Blankenship, R. E.; et al. Comparing Photosynthetic and Photovoltaic Efficiencies and Recognizing the Potential for Improvement. *Science* **2011**, *332*, 805–809.
- (5) Brixner, T.; Stenger, J.; Vaswani, H. M.; Cho, M.; Blankenship, R. E.; Fleming, G. R. Two-Dimensional Spectroscopy of Electronic Couplings in Photosynthesis. *Nature* **2005**, *434*, 625–628.
- (6) Abramavicius, D.; Mukamel, S. Energy-Transfer and Charge-Separation Pathways in the Reaction Center of Photosystem II Revealed by Coherent Two-Dimensional Optical Spectroscopy. *J. Chem. Phys.* **2010**, *133*, 184501.
- (7) Deisenhofer, J.; Michel, H. The Photosynthetic Reaction Center from the Purple Bacterium *Rhodopseudomonas viridis*. *Science* **1989**, *245*, 1463–1473.
- (8) Deisenhofer, J.; Epp, O.; Sning, I.; Michel, H. Crystallographic Refinement at 2.3 Å Resolution and Refined Model of the Photosynthetic Reaction Centre from *Rhodopseudomonas viridis*. *J. Mol. Biol.* **1995**, *246*, 429–457.
- (9) Holzapfel, W.; Finkele, U.; Kaiser, W.; Oesterhelt, D.; Scheer, H.; Stilz, H. U.; Zinth, W. Initial Electron-Transfer in the Reaction Center from *Rhodobacter sphaeroides*. *Proc. Natl. Acad. Sci. U.S.A.* **1990**, *87*, 5168–5172.
- (10) Huppmann, P.; Spörlein, S.; Bibikova, M.; Oesterhelt, D.; Wachtveitl, J.; Zinth, W. Electron Transfer in Reaction Centers of *Blastochloris viridis*: Photosynthetic Reactions Approximating the Adiabatic Regime. *J. Phys. Chem. A* **2003**, *107*, 8302–8309.
- (11) Bixon, M.; Jortner, J. *Advances in Chemical Physics*; John Wiley & Sons, Inc.: New York, 2007; pp 35–202.
- (12) van Brederode, M. E.; van Mourik, F.; van Stokkum, I. H. M.; Jones, M. R.; van Grondelle, R. Multiple Pathways for Ultrafast Transduction of Light Energy in the Photosynthetic Reaction Center of *Rhodobacter sphaeroides*. *Proc. Natl. Acad. Sci. U.S.A.* **1999**, *96*, 2054–2059.
- (13) van Brederode, M. E.; van Grondelle, R. New and Unexpected Routes for Ultrafast Electron Transfer in Photosynthetic Reaction Centers. *FEBS Lett.* **1999**, *455*, 1–7.
- (14) Zhang, W. M.; Meier, T.; Chernyak, V.; Mukamel, S. Exciton-Migration and Three-Pulse Femtosecond Optical Spectroscopies of Photosynthetic Antenna Complexes. *J. Chem. Phys.* **1998**, *108*, 7763–7774.
- (15) Yang, M.; Fleming, G. R. Influence of Phonons on Exciton Transfer Dynamics: Comparison of the Redfield, Foerster, and Modified Redfield Equations. *Chem. Phys.* **2002**, *282*, 163–180.
- (16) Abramavicius, D.; Palmieri, B.; Voronine, D. V.; Sanda, F.; Mukamel, S. Coherent Multidimensional Optical Spectroscopy of Excitons in Molecular Aggregates: Quasiparticle versus Supermolecule Perspectives. *Chem. Rev.* **2009**, *109*, 2350–2408.
- (17) Renger, T. Theory of Optical Spectra Involving Charge Transfer States: Dynamic Localization Predicts a Temperature Dependent Optical Band Shift. *Phys. Rev. Lett.* **2004**, *93*, 188101.
- (18) Makri, N.; Sim, E.; Makarov, D. E.; Topaler, M. Long-Time Quantum Simulation of the Primary Charge Separation in Bacterial Photosynthesis. *Proc. Natl. Acad. Sci. U.S.A.* **1996**, *93*, 3926–3931.
- (19) Bixon, M.; Jortner, J. Electron Transfer via Bridges. *J. Chem. Phys.* **1997**, *107*, 5154–5170.
- (20) Fingerhut, B. P.; Zinth, W.; de Vivie-Riedle, R. Design Criteria for Optimal Photosynthetic Energy Conversion. *Chem. Phys. Lett.* **2008**, *466*, 209–213.
- (21) Abramavicius, D.; Voronine, D. V.; Mukamel, S. Unravelling Coherent Dynamics and Energy Dissipation in Photosynthetic Complexes by 2D Spectroscopy. *Biophys. J.* **2008**, *94*, 3613–9.
- (22) Abramavicius, D.; Zhuang, W.; Mukamel, S. Probing Molecular Chirality via Excitonic Nonlinear Response. *J. Phys. B: At., Mol. Opt. Phys.* **2006**, *39*, 5051.
- (23) Zanni, M. T.; Ge, N.-H.; Kim, Y. S.; Hochstrasser, R. M. Two-Dimensional IR Spectroscopy Can Be Designed to Eliminate the Diagonal Peaks and Expose Only the Crosspeaks Needed for Structure Determination. *Proc. Natl. Acad. Sci. U.S.A.* **2001**, *98*, 11265–11270.
- (24) Huang, L.; Ponomarenko, N.; Wiederrecht, G. P.; Tiede, D. M. Cofactor-Specific Photochemical Function Resolved by Ultrafast Spectroscopy in Photosynthetic Reaction Center Crystals. *Proc. Natl. Acad. Sci. U.S.A.* **2012**, *109*, 4851–4856.
- (25) Lewis, K. L. M.; Ogilvie, J. P. Probing Photosynthetic Energy and Charge Transfer with Two-Dimensional Electronic Spectroscopy. *J. Phys. Chem. Lett.* **2012**, *3*, 503–510.
- (26) Amunts, A.; Drory, O.; Nelson, N. The Structure of a Plant Photosystem I Supercomplex at 3.4 Å Resolution. *Nature* **2011**, *471*, 58–63.
- (27) Abramavicius, D.; Mukamel, S. Exciton Delocalization and Transport in Photosystem I of Cyanobacteria *Synechococcus elongatus*: Simulation Study of Coherent Two-Dimensional Optical Signals. *J. Phys. Chem. B* **2009**, *113*, 6097–6108.
- (28) Umena, Y.; Kawakami, K.; Shen, J.-R. R.; Kamiya, N. Crystal Structure of Oxygen-Evolving Photosystem II at a Resolution of 1.9 Å. *Nature* **2011**, *473*, 55–60.
- (29) Romero, E.; van Stokkum, I. H. M.; Novoderezhkin, V. I.; Dekker, J. P.; van Grondelle, R. Two Different Charge Separation Pathways in Photosystem II. *Biochemistry* **2010**, *49*, 4300–4307.
- (30) Ginsberg, N. S.; Davis, J. A.; Ballottari, M.; Cheng, Y.-C.; Bassi, R.; Fleming, G. R. Solving Structure in the CP29 Light Harvesting Complex with Polarization-Phased 2D Electronic Spectroscopy. *Proc. Natl. Acad. Sci. U.S.A.* **2011**, *108*, 3848–3853.

- (31) Lee, H.; Cheng, Y.-C.; Fleming, G. R. Coherence Dynamics in Photosynthesis: Protein Protection of Excitonic Coherence. *Science* **2007**, *316*, 1462–1465.
- (32) Muller, M. G.; Slavov, C.; Luthra, R.; Redding, K. E.; Holzwarth, A. R. Independent Initiation of Primary Electron Transfer in the Two Branches of the Photosystem I Reaction Center. *Proc. Natl. Acad. Sci. U.S.A.* **2010**, *107*, 4123–4128.
- (33) Koolhaas, M.; van der Zwan, G.; van Mourik, F.; van Grondelle, R. Spectroscopy and Structure of Bacteriochlorophyll Dimers. I. Structural Consequences of Nonconservative Circular Dichroism Spectra. *Biophys. J.* **1997**, *72*, 1828–1841.
- (34) Won, Y.; Friesner, R. A. Simulation of Optical Spectra from the Reaction Center of *Rhodopseudomonas viridis*. *J. Phys. Chem.* **1988**, *92*, 2208–2214.
- (35) Parson, W. W.; Chu, Z.-T.; Warshel, A. Electrostatic Control of Charge Separation in Bacterial Photosynthesis. *Biochim. Biophys. Acta* **1990**, *1017*, 251–272.
- (36) Parson, W. W.; Chu, Z. T.; Warshel, A. Reorganization Energy of the Initial Electron-Transfer Step in Photosynthetic Bacterial Reaction Centers. *Biophys. J.* **1998**, *74*, 182–191.